Soft Matter

Polymer solution structure and dynamics within pores of hexagonally close-packed nanoparticles

Journal:	*Soft Matter*
Manuscript ID	SM-ART-08-2022-001102.R1
Article Type:	Paper
Date Submitted by the Author:	22-Sep-2022
Complete List of Authors:	Heil, Christian; University of Delaware, Newark, Chemical and Biomolecular Engineering Jayaraman, Arthi; University of Delaware, Chemical and Biomolecular Engineering

Submitted to Soft Matter

Polymer solution structure and dynamics within pores of hexagonally close-packed nanoparticles†

Christian M. Heil[1], Arthi Jayaraman[1,2,*]

[1]Department of Chemical and Biomolecular Engineering, 150 Academy St., University of Delaware, Newark, DE 19716. United States of America

[2]Department of Materials Science and Engineering, 201 DuPont Hall, University of Delaware, Newark, DE 19716. United States of America

*Corresponding author arthij@udel.edu

†Electronic supplementary information (ESI) available.

Abstract:

Using coarse-grained molecular dynamics simulations, we examine structure and dynamics of polymer solutions under confinement within the pores of a hexagonally close-packed (HCP) nanoparticle system with nanoparticle diameter fifty times that of the polymer Kuhn segment size. We model a condition where the polymer chain is in a good solvent (i.e., polymer-polymer interaction is purely repulsive and polymer-solvent and solvent-solvent interactions are attractive) and the polymer-nanoparticle and solvent-nanoparticle interactions are purely repulsive. We probe three polymer lengths (N = 10, 114, and 228 Kuhn segments) and three solution concentrations (1, 10, and 25%v) to understand how the polymer chain conformations and chain center-of-mass diffusion change under confinement within the pores of the HCP nanoparticle structure from those seen in bulk. The known trend of bulk polymer R_g^2 decreasing with increasing concentration no longer holds when confined in the pores of HCP nanoparticle structure; for example, for the 114-mer, the HCP $<R_g^2>$ at 1%v concentration is lower than HCP $<R_g^2>$ at 10%v concentration. The $<R_g^2>$ of the 114-mer and 228-mer exhibit the largest percent decline going from bulk to HCP at the 1%v concentration and the smallest percent decline at the 25%v concentration. We also provide insight into how the confinement ratio (CR) of polymer chain size to pore size within tetrahedral and octahedral pores in the HCP arrangement of nanoparticles affects the chain conformation and diffusion at various concentrations. At the same concentration, the N = 114 has significantly more movement between pores than the N = 228 chains. For the N = 114 polymer, the diffusion between pores (i.e., inter-pore diffusion) accelerates the overall diffusion rate for the confined HCP system while for the N = 228 polymer, the polymer diffusion in the entire HCP is dominated by the diffusion within the tetrahedral or octahedral pores with minor contributions from inter-pore diffusion. These findings augment the fundamental understanding of macromolecular diffusion through large, densely packed nanoparticle assemblies and are relevant to research focused on fabrication of polymer composite materials for chemical separations, storage, optics, and photonics.

We perform coarse-grained molecular dynamics simulations to understand structure and dynamics of polymer solutions under confinement within hexagonal close packed nanoparticles with radii much larger than the polymer chain's bulk radius of gyration.

Keywords:

Polymer nanocomposite, confinement, nanoparticles, polymer solution, polymer diffusion

I. Introduction

Polymer nanocomposites (PNC) are a class of soft materials comprised of a polymer matrix and nanoscale fillers (e.g., organic or metallic nanospheres, nanorods, nanotubes or nanosheets). PNCs are synthetically engineered as well as found in nature. For example, in nature, many organisms produce color from the arrangement of melanin particles (melanosomes) in a matrix of other biological macromolecules (e.g., keratin).[1] In various industries, PNCs are engineered for applications (e.g., vehicle parts, aircraft parts, tires, packaging) that take advantage of the enhanced properties (e.g., improved mechanical and/or thermal properties, increased barrier to small molecule diffusion) brought about by the mixing of the nanofillers and polymer.[2, 3] While past computational work and experiments have been focused on studying PNCs with nanofillers being the minority component, there is a push for engineering PNCs with larger nanofiller content (e.g., >50%vol filler) as it has been found that the nanofiller-induced polymer confinement improves PNC toughness.[4, 5] One approach to fabricate PNCs with higher filler content is through a solvent casting process whereby the nanofiller and polymer are mixed in the desired portions in a solvent, and upon solvent evaporation, one forms PNCs with the desired composition.[6-8] For such processes, there is a need to focus on polymer structure and dynamics around nanofillers in the presence of solvent and to study how the evaporation of the solvent affects the polymer structure and dynamics; the former is tackled in this paper.

Structure and dynamics in *bulk* polymer solutions have been the focus of many past studies (experimental and theoretical) that led to well-established expressions for scaling of the polymer diffusion coefficient, polymer radius of gyration, and solution viscosity with varying polymer chain length and concentration.[9-11] Structure and dynamics of polymers in confinement have been studied in the context of PNCs where the additive nanoparticle is the minority component (1-15%

by volume) and the polymer chains are the majority component.[12-17] Studies focused on PNCs with minority component nanoparticles (NPs) found that the polymer conformation is unperturbed by the presence of spherical nanoparticles when the polymer-NP interaction is repulsive[18-20] and that an attractive polymer-NP interaction can cause polymer conformation to expand,[21-23] contract,[24] or remain unperturbed.[18, 25] For cases of large nanoparticles whose size is much larger than the polymer chain size, past work has applied the Asakura-Oosawa model to confined polymer solutions in the presence of such large (minority component) nanoparticles.[26-30] However, the Asakura-Oosawa model treats the polymer as an ideal polymer[31] which may not be applicable for strongly confined polymers where the degree of confinement causes significant deviation from the ideal polymer chain conformation.

To understand polymer diffusion under extreme confinement, researchers have investigated the "entropic barrier" to polymer diffusion theory in model systems.[32-36] This work focused on considering a polymer chain as it diffuses through a small hole or around periodic obstacles. These studies found that polymer diffusion (D) scaling with polymer length (N) has three distinct regimes depending on the polymer concentration and presence of entropic barriers: the Rouse regime, the entropic barrier regime, and the reptation regime. While the Rouse regime and reptation regime have well defined diffusion scaling of $D \sim N^{-1}$ and $D \sim N^{-2}$ respectively (applicable for non-barrier systems based on entangled vs. unentangled polymers), the entropic barrier regime generally has a stronger polymer length dependence with a scaling exponent of -2 to -3.[33] However, the scaling exponent can also be less than -1 depending on the system because "the apparent exponent that is extracted in this regime is non-universal and depends on the specific problem. In fact, the different values of the [scaling] exponent α observed experimentally by different investigators are a direct result of their experimental situation belonging to this crossover

regime" (quoted from Ref.[33]). This finding justifies the need for further work to investigate polymer solutions in complex confinements as the dynamic scaling laws are likely to vary based on the confinement. While the past work focused on model (extreme) confinement systems,[32-36] there is also interest in understanding the impact of complex confinement topology on polymer diffusion caused by realistic nanoparticle packing within PNCs at high nanoparticle loading. Experimental work on PNCs with high nanoparticle loading and small inter-nanoparticle distances (related to entropic bottleneck size) found that the polymer diffusion rate did not match either the Rouse or reptation scaling expectation but instead matched that for an entropic barrier (though the slope value from ~1.5-2 demonstrates that predicting the slope for complex topographies is non-intuitive).[37] Simulation work on polymer diffusion through a monolayer of nanoparticles with varying interparticle distances (and by extension confinement) found that polymer conformations are strongly perturbed when the distance between nanoparticles forming the monolayer is less than twice the polymer radius of gyration.[38] Furthermore, the authors noted that the polymer diffusion through the nanoparticle monolayer is slower with increasing confinement (smaller distance between nanoparticles), matching the entropic barrier theory.[38]

There are multiple other studies also focused on understanding polymer structure and dynamics with nanoparticles as the majority component (>50% volume) with the polymer (no solvent) as the minority component occupying the gaps or pores between nanoparticles where the polymer chains feel strong confinement.[13, 37-50] Studies found that increasing the confinement relative to the polymer size significantly increased viscosity,[42] and the polymer-nanoparticle interaction strength effect (weakly or strongly attractive) was negligible compared to the confinement effect.[43] Experimental work found that the pore shape (concave as found in nanoparticle assemblies or convex as found in cylindrical pores) impacts polymer dynamics with

concave pores having a higher glass transition temperature than convex pores, indicating slower dynamics for concave pores.[46] This work[46] further suggests that the polymer dynamics in nanoparticle assemblies are not easily extrapolated from the more well-defined nanopore structures examined in other works. Further experimental work investigated polymer infiltration rates into nanoparticle assemblies, and the authors found that the polymer infiltration rate significantly slowed as the degree of confinement increased.[44] Interestingly, the extent of infiltration was independent of the confinement degree with strongly confined to even more strongly confined polymers achieving a similar extent of infiltration.[44] Thus, one would expect the majority of the changes to polymer dynamics to occur when the degree of confinement is closer to one, indicating similar polymer and pore size. Molecular dynamics (MD) simulations were employed to investigate the polymer infiltration into a disordered nanoparticle assembly while varying polymer-nanoparticle interactions.[39] Interestingly, these authors found that adjusting the nanoparticle-polymer interaction resulted in two different diffusion modes. A strongly attractive nanoparticle-polymer interaction resulted in adhesion-dominated transport where the adsorbed polymers slowly but steadily work their way into the assembly, and a weakly attractive nanoparticle-polymer interaction resulted in dissolution-dominated transport where the polymer rapidly diffused through the nanoparticle pores.[39] The authors found an intermediate interaction strength had the fastest diffusion because too strong polymer-nanoparticle attraction results in polymer adhesion/sticking to nanoparticle.[39] Other MD work examined the impact of polymer concentration (polymer filler fraction) on these high filler loading PNCs for both unentangled and entangled polymer chains for attractive polymer-nanoparticle interactions.[45] The authors found that the higher the number of nanoparticle contacts, the larger the slowdown in monomer segmental dynamics.[45] Additionally, confinement reduced the density of entanglements matching

previous work that found high confinement reduced entanglements (eventually leading to polymer disentanglement).[45] While the previous work focused on polymer structure and dynamics in majority nanoparticle PNCs (no solvent),[13, 37-50] there is a lack of understanding on how strong confinement affects polymer *solution* structure and dynamics.

In this article, we seek to understand (minority component) polymer chains' structure and dynamics in polymer solutions within a hexagonally close packed (HCP) crystalline arrangement of (majority component) nanoparticles with diameters significantly larger than the polymer chains' radii of gyration. We first elucidate the change in polymer chain structure and dynamics going from a bulk solution (no nanoparticles) to a confined state (around nanoparticles packed in a hexagonally close-packed crystalline arrangement). We focus on polymer chains with radii of gyration similar to the pore radius between the nanoparticle crystals. For sufficiently large polymer confinement, we find that polymer structure is most collapsed for the dilute polymer with semi-dilute polymers maintaining larger sizes and that semi-dilute polymer dynamics no longer decrease with increasing polymer concentration. We examine how the type of HCP pore, tetrahedral or octahedral, significantly impacts the localization of polymer beads inside the pore and dynamics of polymer beads moving between pores. We further investigate how polymer structure and dynamics in individual tetrahedral and octahedral pores are similar or different from those in an HCP crystal.

The paper is organized as follows. In **Section II**, we describe the model, MD simulation details, analyses performed, and the parameter space explored. In **Section III**, we present and discuss the simulation results. In **Section IV**, we provide concluding remarks based on key results in this work.

II. Computational Approach

A. Model:

We employ a coarse-grained (CG) approach to model the polymer, solvent, and nanoparticles. We represent the polymer as a linear flexible bead-spring[51] chain (**Figure 1a**). A polymer is comprised of N number of CG beads each of diameter 1 d equal to the Kuhn length of the polymer. We study three chain lengths of $N = 10$, $N = 114$, and $N = 228$ Kuhn segments that are selected to have polymer sizes (radius of gyration) well below ($N = 10$), around ($N = 114$) and almost twice ($N = 228$) the pore sizes in the HCP nanoparticles. These CG beads are connected together using the finitely extensible nonlinear elastic (FENE) bond potential with spring constant ($k = 30\ kT/d^2$) and maximum spring extension ($r_0 = 1.5\ d$).[51] The FENE bond potential is used as it has been shown to correctly capture polymer dynamics.[52] For these explicit solvent simulations, we model the solvent as CG beads of diameter 1 d. Depending on the density of the solvent represented, one can convert 1 CG bead to the n solvent molecules it collectively represents. We set the mass of each polymer CG bead as $m = 1$ (normalized units). The mass of the solvent CG bead is scaled based on the density of the polymer and solvent; in this study we use polyvinyl alcohol in water as an example, making the mass for each solvent CG bead equal to 1.25 m. Each 50 d diameter nanoparticle is modeled as a rigid body collection of 0.5 d diameter beads; for simplicity these 0.5 d beads are arranged in a hexagonally close packed (HCP) crystal (**Figure 1a**); the 0.5 d bead size enables the nanoparticles to have fewer edges and be more curved. In the cubic simulation box of size 80 d, multiple 50 d nanoparticles are placed in an HCP arrangement (**Figure 1b**). For an ideal HCP crystalline arrangement, the pores are either tetrahedral or octahedral, where the tetrahedral pores are smaller in volume but more numerous than the octahedral pores. Both the tetrahedral and octahedral pores possess a concave shape due to the pore being formed around

spherical nanoparticles. Tetrahedral pores have a pore radius that is ~22.5% of the nanoparticle radius, and octahedral pores have a pore radius that is ~41.4% of the nanoparticle radius (**ESI Table S1**).[53] The pore radius is defined from the largest sphere centered in the pore that does not overlap the surrounding nanoparticles.[53] The simulation box size of 80 *d* is selected to be sufficiently large to obtain structural and dynamical information about the polymer within multiple pores of the HCP crystal and small enough to be computationally feasible to simulate polymer solutions with explicit solvent representation.

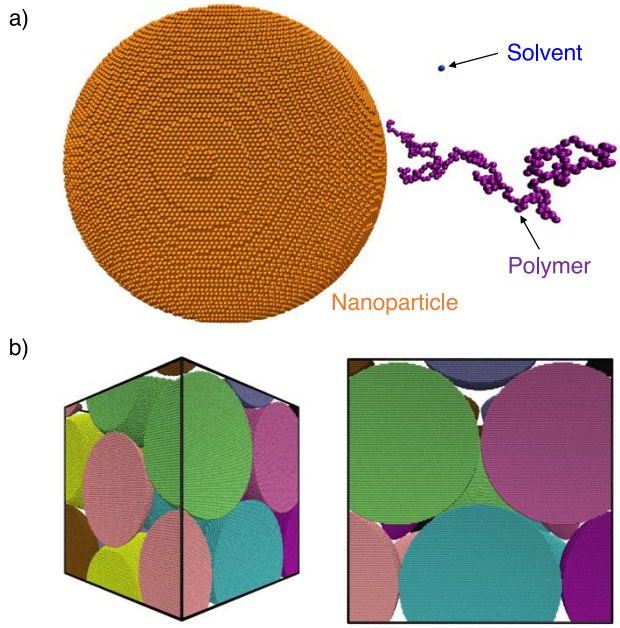

Figure 1*: a) CG model of nanoparticle (of diameter 50 d), solvent (of diameter 1 d), and a polymer chain (of 1 d diameter beads), drawn to scale. b) Two views of the simulation set up of the nanoparticle hexagonal close packing with each nanoparticle individually colored for better visualization. The side length of the simulation box of the nanoparticle crystal is 80 d.*

For the polymer and solvent CG beads, we model non-bonded, pairwise interactions using the expanded form of the Lennard Jones[54] (LJ) potential with $\varepsilon_{ij} = 1.0$, $\sigma_{ij} = 1\ d$, and Δ_{ij} set to $0\ d$ based on the diameters of the pairs of beads considered. For the polymer-solvent and solvent-

solvent cases, we set $r_{cut} = 2.5\ \sigma_{ij}$, and for the polymer-polymer case, we set $r_{cut} = 2^{1/6}\ \sigma_{ij}$ (purely repulsive) to mimic a condition where the solvent is a good solvent for the polymer. We use the expanded LJ potential for interactions between the polymer and solvent with the nanoparticle subunits (0.5 *d* beads). We set $\varepsilon_{ij} = 1.0$, $\sigma_{ij} = 1\ d$, Δ_{ij} to -0.25 *d* based on the diameters of the polymer, solvent, and nanoparticle subunit beads, and r_{cut} to $2^{1/6}\ \sigma_{ij}$ to model repulsive polymer-nanoparticle and solvent-nanoparticle interactions. We use the expanded LJ potential form because it allows all interactions to maintain the same "hardness" regardless of whether we study bulk polymer solutions or polymer solutions under confinement. The expanded LJ potential form ensures the same "hardness" by maintaining the same σ_{ij} to ensure the potential slope is consistent for all interactions and uses the Δ_{ij} to shift the potential minimum to account for different bead sizes (see **ESI Figure S1)** .

B. Simulation Method:

We perform molecular dynamics (MD) simulations using the LAMMPS package.[55] For the unconfined (i.e., no nanoparticles) 'bulk' simulations, we use a cubic simulation box with side length of 78 *d*, which is greater than three times the radius of gyration of the longest polymer chain considered (N = 228) to prevent unphysical polymer self-interaction. We determine the total number of CG polymer and solvent beads by calculating the number of 1 *d* diameter beads required to achieve a 0.7 d^{-3} bead number density to mimic a liquid. Once we know the total number of CG beads, we then determine the number of polymer chains of length N to achieve the correct polymer volume percent of 1%v, 10%v, or 25%v (where the exact percent may vary slightly as every polymer chain must be N beads long). The remaining beads are designated as solvent beads. To

determine whether the polymer solution is dilute or semi-dilute, we calculate the polymer overlap concentration c^* as:

$$c^* = \frac{3N}{4\pi\left(R_{g0}{}^2\right)^{3/2}} \quad (1)$$

$$R_{g0}{}^2 = N^{2\nu} \quad (2)$$

with ν found to be ~0.61 by fitting Equation 2 to the simulation results, in agreement with scaling exponent of polymers in good solvent seen in previous work.[9-11] For each system, we calculate the polymer bead concentration c as the number of beads per chain times the number of chains in the simulation box divided by the total available volume. We call a system dilute if c/c^* is less than one and we call the solution semi-dilute if c/c^* is above one. For reference, the $N = 10$ systems are dilute for 1%v, 10%v, and 25%v. The $N = 114$ and $N = 228$ systems are dilute for 1%v and semi-dilute for 10%v and 25%v.

For these bulk simulations, the polymer chains and solvent beads are randomly placed in the cubic simulation box and undergo an energy minimization for ~$1\text{x}10^4$ timesteps (each timestep $dt = 0.005\ \tau$) to remove any overlaps before equilibration. This timestep size is chosen because a larger timestep size causes the simulation to crash due to bond breaking, and a smaller timestep size increases the number of timesteps required for equilibration without any additional benefit. We equilibrate the system for a number of timesteps equal to at least ten times the time needed for the polymer end-to-end vector to become uncorrelated. To do this, we calculate the polymer chain end-to-end vector (R_{ee}) autocorrelation function (ACF):

$$ACF(R_{ee}) = \frac{R_{ee}(t) \cdot R_{ee}(0)}{R_{ee}(0) \cdot R_{ee}(0)} \quad (3)$$

where $R_{ee}(0)$ is the polymer chain end-to-end vector at the initial time $t = 0$ and $R_{ee}(t)$ is the polymer chain end-to-end vector at time t. The time needed for the ACF to approach zero is taken as the

time needed for the system configuration to be uncorrelated. The longest time is ~5,000 τ for the N = 10 systems, ~150,000 τ for the N = 114 systems, and ~500,000 τ for the N = 228 systems.

After the equilibration, we sample configurations during the production stage for ~5x10^8 timesteps at T^* = 1 in the NVT ensemble with a Nose-Hoover thermostat with the LAMMPS thermostat damping parameter τ_{damp} = 0.5 τ. The exact number of timesteps during sampling is based on the time needed to sample a sufficient number of uncorrelated structures at regular time intervals to determine the polymer dynamics. For all bulk simulations, we perform three independent trials for each condition.

For the systems of a polymer solution confined within the HCP nanoparticle crystal, we generate a simulation box centered around one of the nanoparticles with a cubic box side length of 1.6 times the nanoparticle diameter or 80 d, and we remove any parts of the crystal that extend beyond the simulation box. This box size is large enough for the polymer chains to sample multiple pores in the HCP nanoparticle crystal without any simulation box size effects on structure and dynamics and at the same time small enough for these simulations with explicit solvent to be computationally feasible. For simulations of the individual tetrahedral and octahedral pores, we center a simulation on a single pore with the simulation box set to 5 d larger than the pore diameter to fully encompass the pore (**ESI Table S1** and **ESI Figure S2**). To understand the long-time diffusion of the polymer in the individual tetrahedral and octahedral pores, we allow the simulation box to be periodic whereby the polymer exiting from one end of the pore reappears on the other end of the simulation box. To focus on the polymer structure and dynamics, we restrict the nanoparticles from moving as they are already assembled into a crystal.

For both the entire HCP simulation and the individual pores simulations, we determine the total number of CG solvent beads to achieve the correct number density required to mimic a liquid

solvent by progressively adding solvent beads into the simulation box and equilibrating until the solvent-solvent pair correlation function g(r) in confinement matches the solvent-solvent g(r) for an unconfined, bulk liquid solvent. Once we determine the total number of CG solvent beads, a fraction of those CG solvent beads is replaced with the number of CG polymer beads that leads to the correct polymer volume fraction. Then from that number we find the number of polymer chains of length N to achieve the desired polymer volume fraction. The CG polymer beads and solvent beads are randomly placed in the simulation box avoiding overlap with the nanoparticles. The system undergoes an energy minimization for ~$1x10^4$ timesteps (each timestep $dt = 0.005\ \tau$) after placement to remove any bead overlap. An equilibration occurs for ten times the polymer end-to-end vector de-autocorrelation time (which as stated above depends on the chain length N), and then, we perform sampling for ~$5x10^8$ timesteps. All simulations are conducted at $T^* = 1$ in the NVT ensemble using a Nose-Hoover thermostat with the LAMMPS thermostat damping parameter $\tau_{damp} = 0.5\ \tau$. As with the bulk simulations, the exact number of timesteps is varied to ensure we sample the long-time, diffusive polymer regime. For all confined simulations, we perform three independent trials for all systems except we conduct ten independent trials for the N = 228, 1 vol% system because it possesses few polymer chains, requiring more trials to achieve good statistics.

For both bulk and confined systems, we confirm equilibration by simulating for at least 10 times the polymer end-to-end vector relaxation time and by ensuring the polymer center of mass (COM) diffuses at least twice the squared radius of gyration.[56] We also ensure that our bulk polymer solutions reproduce the well-known structural (radius of gyration) and dynamical (polymer relaxation time) scaling as the polymer solution concentration (%v) and chain length (N) are varied.[9-11] We provide the relevant validations in **ESI Section SII** and **ESI Figure S3**.

C. Analyses:

We calculate the polymer chains' conformation through their squared radius of gyration (R_g^2); changes in the R_g^2 value going from bulk to the confined systems describe the conformational change caused by confinement. We calculate the polymer COM mean squared displacement (MSD) to determine how the polymer diffusion coefficient varies in confinement compared to bulk. Using the MSD, we calculate the polymer COM diffusion coefficient (D) using the Einstein diffusion relationship[56]

$$D = \frac{1}{6}\lim_{t\to\infty}\frac{d}{dt}\left\langle \frac{1}{N_{polymer}}\sum_{i=1}^{N_{polymer}}\left(COM_i(t) - COM_i(0)\right)^2\right\rangle \quad (4)$$

with $N_{polymer}$ the number of polymers in the system and $COM_i(t)$ the i-th polymer center of mass at time t.

To quantify the extent of polymer confinement in the HCP nanoparticle crystal, for each chain length N, we calculate the 'confinement ratio' (CR) as the bulk polymer R_g (calculated from bulk MD simulations) divided by the tetrahedral and octahedral pore sizes (**ESI Table S1**) within the HCP crystal (**Table 1**). When polymer chain moves between the tetrahedral and octahedral pores, it experiences confinement equal to the inter-pore size as the radius of the hole in the plane formed by the three touching nanoparticles.

$$R_{inter-pore} = \left(\frac{2}{sqrt(3)} - 1\right)R_{Nanoparticle} \quad (5)$$

***Table 1**: Confinement ratio (CR) experienced by polymer for all systems in this work.*

N (polymer length)	%v (polymer concentration)	$\langle R_g^2\rangle$ bulk $[d^2]$	CR $_{\text{Tetrahedral}}$	CR $_{\text{Octahedral}}$	CR $_{\text{Inter-pore}}$
10	1	3.02 ± 0.82	0.31	0.17	0.45
10	10	2.97 ± 0.81	0.31	0.17	0.45
10	25	2.85 ± 0.80	0.30	0.16	0.43
114	1	90.4 ± 63.8	1.69	0.93	2.49

114	10	74.6 ± 54.8	1.54	0.84	2.25
114	25	60.1 ± 43.3	1.38	0.76	2.03
228	1	210.0 ± 151.3	2.58	1.41	3.77
228	10	158.9 ± 119.6	2.24	1.23	3.29
228	25	123.6 ± 88.1	1.98	1.08	2.89

To understand the polymer behavior in the HCP confined simulation systems, we determine the type of pore (tetrahedral or octahedral) that each polymer bead is closest to (accounting for the different pore sizes) for each snapshot. This allows us to understand which pores have the highest polymer bead localization as well as which pores tend to exchange more polymer beads between snapshots. To understand polymer bead motion between pores, we determine which polymer beads are closest to a different pore after the snapshot time interval of 156,250 τ and mark the original and new pore as having a polymer bead move in/out of the pores. We quantify the number of solvent beads contacting the polymer by counting the number of unique solvent beads that were within 1.5 *d* of the polymer beads in the polymer chain. For all plots, error bars represent the standard error of the mean for all replicates across all simulation outputs. All visualizations are provided using the VMD software.[57]

III. Results and Discussion

We first discuss the results comparing the polymer structure and dynamics under confinement in the HCP nanoparticle crystal to bulk polymer structure and dynamics. Initially, we consider the overall polymer structure and dynamics in the HCP before elucidating the polymer localization and movement between the tetrahedral and octahedral pores within the HCP nanoparticle crystal. Finally, we compare the polymer structure and dynamics from simulations of a specific tetrahedral and octahedral pore to the structure and dynamics of the polymer within the HCP nanoparticle crystal.

A. Comparing polymer structure and dynamics under HCP confinement to bulk:

We consider the polymer structure, quantified by the polymer R_g^2, for all polymer lengths and polymer concentrations in this study in **Figure 2**. We first examine the shortest polymer length (N = 10) that has the smallest confinement effect; for the 10-mer at all concentrations, the CR is 0.15-0.45 (**Table 1**) meaning the polymer is smaller than all pore radii within the HCP. In **Figure 2a** and **Figure 2b**, both the R_g^2 probability distribution and the ensemble average $\langle R_g^2 \rangle$ demonstrate that the polymer structure does not change much going from bulk to HCP crystal simulations for all polymer concentrations. We note that the $\langle R_g^2 \rangle$ for the confined polymer solutions is slightly below that for the bulk polymer solutions. The $\langle R_g^2 \rangle$ trend with increasing concentration is consistent for both confined and bulk systems with $\langle R_g^2 \rangle$ decreasing with increasing polymer concentration.

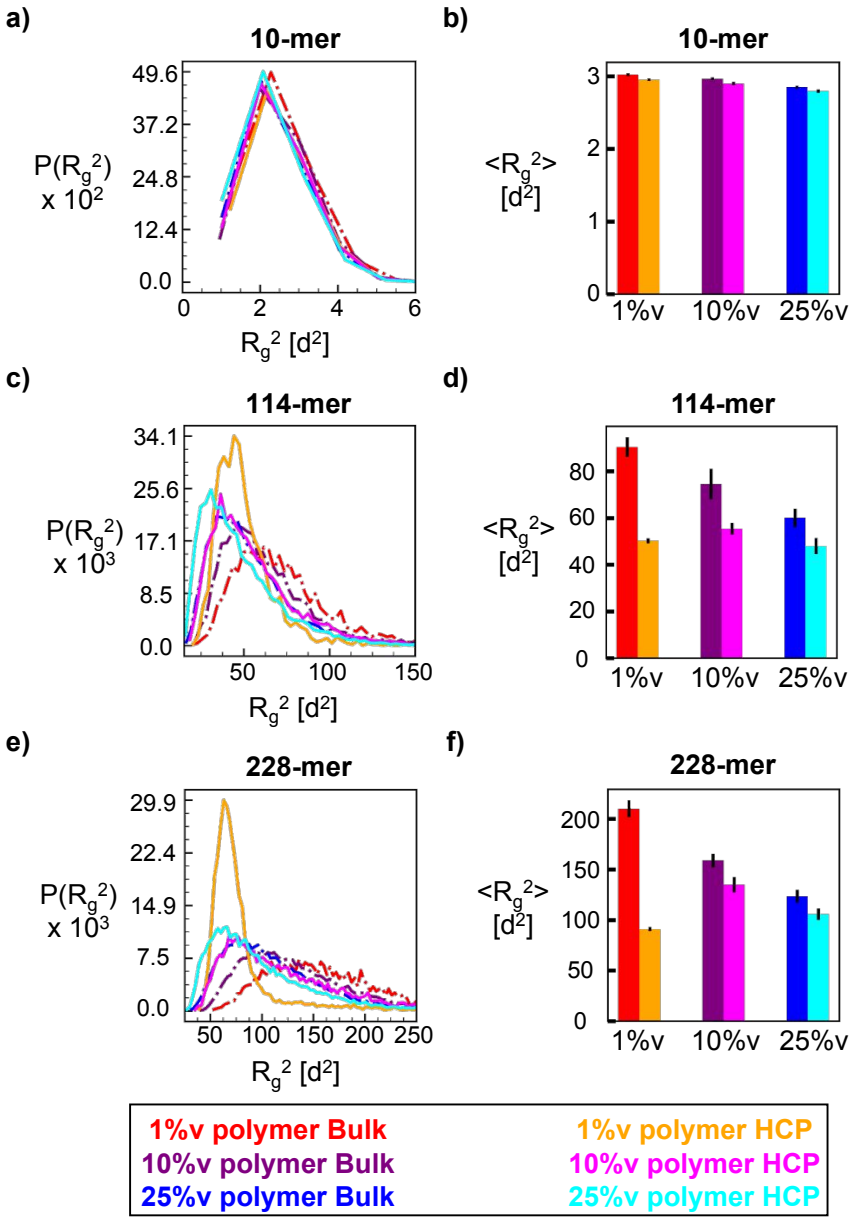

***Figure 2**: Polymer radius of gyration for bulk polymer solutions and confined polymer solutions. a), c), and e) provide the squared polymer radius of gyration probability distribution as a function of the squared radius of gyration. b), d), and f) depict the ensemble averaged radius of gyration squared. a) and b); c) and d); and e) and f) are for N = 10, N = 114, and N = 228 polymer solutions respectively. The red and orange colors are the 1%v polymer solution in bulk and under HCP confinement respectively. The dark purple and magenta colors are the 10%v polymer solution with the dark purple representing the bulk and the magenta representing the confined systems. The dark blue and cyan colors are for the 25%v polymer solution in bulk and confinement respectively. The bulk systems in a), c), and e) are plotted with a dot-dash line. The error bars for b), d), and f) are the standard error of the mean of 3 independent replicates except for the N = 228, 1%v polymer concentration under HCP confinement where it is the standard deviation of 10 independent replicates.*

In **Figure 2c** and **Figure 2d**, we consider the intermediate polymer length (N = 114) that experiences a CR of ~0.8-1.5 in tetrahedral and octahedral pores (**Table 1**) which means the polymer $<R_g>$ is commensurate with the tetrahedral and octahedral pore radii. At this CR, we expect the confinement to induce a perturbation from the bulk polymer structure especially at lower polymer concentration. The R_g^2 probability distribution (**Figure 2c**) indicates that the 114-mer polymers tend to adopt a smaller conformation under confinement, and the lack of a secondary peak at large R_g^2 suggests that the polymer conformation is not bimodal with two distinct groups of polymers with different structures. Further, the known trend of bulk polymer R_g^2 decreasing with increasing concentration[9-11] no longer holds under HCP confinement; the HCP $<R_g^2>$ of the 114-mer at 1%v concentration is lower than HCP $<R_g^2>$ of the 114-mer at 10%v concentration. The $<R_g^2>$ of the 114-mer exhibits the largest percent decline going from bulk to HCP at the 1%v concentration (declining 44.5%) and the smallest percent decline at the 25%v concentration (decreasing 20.1%).

In **Figure 2d**, the $<R_g^2>$ trend with increasing concentration is now non-monotonic for the confined system with $<R_g^2>$ smallest for low concentration, highest for intermediate concentration, and then decreasing at higher concentration. The decrease in the $<R_g^2>$ from 10%v to 25%v for the confined system follows a similar trend as in bulk; however, the increase in the $<R_g^2>$ for the confined system from lowest polymer concentration 1%v to 10%v differs from the trend in bulk. We believe this is because of the stronger confinement effect at the lowest polymer concentration. In bulk, in a good solvent at the lowest polymer concentration, one would expect to see extended polymer chains with minimal crowding from other chains; in contrast, in confinement, these polymer chains now are geometrically frustrated by the repulsive walls of the pore driving them to collapsed configurations to fit within the space between nanoparticles (since the CR is near

unity). Furthermore, given the same repulsive polymer-nanoparticle and solvent-nanoparticle interactions, we expect solvent beads to preferentially segregate near the pore wall as compared to the polymer beads; this is based on past literature on binary polymer blends of differing lengths near an interface demonstrating that the shorter polymer concentrates at the interface with the degree of segregation increasing as the longer chain length to shorter chain length ratio increases.[58] Thus for our polymer solution, we expect a similar situation with the solvent preferentially segregated to the pore surface, forcing the polymer to collapse within the center of the pore. Also, as will be discussed in **Figure 3**, the lowest polymer concentration systems possess the slowest diffusivity, meaning the polymer chains remain collapsed within the HCP pores instead of stretching out to move between pores, further explaining the reduced $<R_g^2>$. As the polymer concentration increases, due to the presence of other polymer chains in solution, the polymer chains are driven out of pores (in extended configurations) rather than collapsing in the center of the pore. These are the likely reasons causing the non-monotonic behavior in 114-mer polymer $<R_g^2>$ for chains in HCP confinement with varying polymer concentration.

We also examine the number of solvent beads contacting the polymer chain in bulk and in HCP confinement (**ESI Figure S4**). We find that in the bulk for all N, the number of solvent bead contacts per chain decreases with increasing polymer concentration, as one may expect. However, under HCP confinement, that trend is reversed with the number of solvent bead contacts per chain increasing with polymer concentration for all N considered. Furthermore, the average number of solvent bead contacts is higher for the confined polymer than the bulk polymer with the greatest deviation at the highest polymer concentration. We explain these counter-intuitive trends of decreasing $<R_g^2>$ going from bulk to HCP along with increasing solvent contacts going from bulk to HCP as follows. Because we model a polymer in a good solvent (attractive polymer-solvent

interaction) with repulsive polymer-nanoparticle and repulsive solvent-nanoparticle interactions, we attribute these trends to the solvent beads forming a layer around the polymer to shield the solvent and polymer beads from the repulsive nanoparticle. Thus, the large decrease in $<R_g^2>$ under confinement does not result in a subsequent decrease in solvent-polymer contacts.

The final polymer length considered ($N = 228$) has a CR above unity (**Table 1**) indicating this polymer R_g is larger than all the HCP pore radii. Similar to the other polymer lengths considered, the $N = 228$ polymer has a unimodal R_g^2 distribution as seen in **Figure 2e**. Similar to the $N = 114$ polymer, this $N = 228$ polymer undergoes the largest decrease of $<R_g^2>$ from bulk to HCP confinement at the lowest concentration (**Figure 2f**); the $<R_g^2>$ for the 228-mer 1%v system declines by 56.7% going from bulk to confined while the $<R_g^2>$ for the 25%v system decreases by 14.4% going from bulk to confined.

Thus, as the CR increases between the $N = 114$ and $N = 228$ polymer systems, the $<R_g^2>$ for the 1%v concentration exhibits a greater percent decline for the polymer with the higher CR, and the $<R_g^2>$ for the 25%v concentration polymer solution undergoes a smaller percent decline for the polymer with the higher CR.

In **Figure 3**, we compare the COM polymer diffusion coefficient, D, in bulk and under HCP confinement. When we examine polymer diffusion, we find that even the least confined $N = 10$ polymer experiences a reduction in its diffusion rate under HCP confinement as seen in **Figure 3a**. For the bulk solutions, D monotonically decreases with increasing polymer concentration as one would expect;[9-11] however, for the HCP confined solutions, the polymer exhibits a completely different trend with increasing polymer concentration. Under confinement, the 1%v concentration system exhibits a drastically reduced diffusion rate that is substantially less than the 10%v and 25%v systems while the 10%v and 25%v polymer solutions achieve similar diffusion rates. We

attribute this difference at low polymer concentrations (1%v) to an insufficient 'drive' to force the polymer to stretch out and transition between pores. At low polymer concentrations, most polymer contacts are the energetically favorable polymer-solvent contacts, balancing the entropic penalty of remaining in a pore; at higher polymer concentrations, there are an increasing number of repulsive polymer-polymer contacts and macromolecular crowding that then help 'drive' the polymer between pores. Thus, going from 10%v to 25%v, we likewise observe a slight increase in polymer diffusivity. When we consider longer polymer chains in **Figure 3b** and **Figure 3c**, we observe a similar trend as that found in the $N = 10$ system with a more pronounced confined diffusivity increase at higher polymer concentration than the $N = 10$ system. We note that the relative decline in the polymer diffusion going from bulk to HCP confinement decreases as the N increases. As shown in **ESI Figure S5**, these trends seen with D are consistent with the polymer MSD curves.

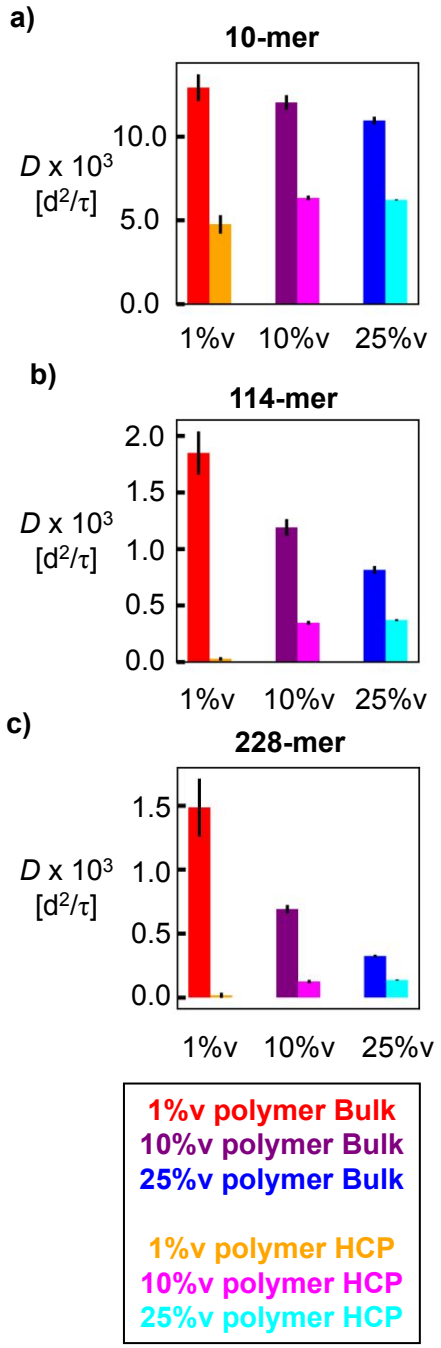

***Figure 3**: Polymer diffusion coefficient (D) for bulk polymer solutions and confined polymer solutions. a), b), and c) are the polymer diffusion coefficient for N = 10, N = 114, and N = 228 polymer solutions respectively. The red and orange colors are the 1%v polymer solution in bulk and under HCP confinement respectively. The dark purple and magenta colors are the 10%v polymer solution with the dark purple representing the bulk and the magenta representing the confined systems. The dark blue and cyan colors are for the 25%v polymer solution in bulk and confinement respectively. The error bars are the standard error of the mean of 3 independent*

replicates except for the N = 228, 1%v polymer concentration under HCP confinement where it is the standard deviation of 10 independent replicates.

To understand the role of the tetrahedral and octahedral pores in the HCP confined system on the polymer localization and dynamics, we determine the closest pore location for all polymer beads (**Figure 4**). We focus on polymer lengths of N = 114 and N = 228 and polymer concentrations of 10%v and 25%v as these polymer lengths experience the greatest degree of confinement in the HCP crystal, and the higher polymer concentrations exhibit unexpected behavior under confinement. Furthermore, the thermal blob size for this system is ~7.3 *d* (**ESI Section SII**) which is larger than the R_g of all $N = 10$ systems indicating that the $N = 10$ systems are not in the swelling regime.

We first consider which type of pore, on average, the polymer beads tend to be closest to. We show the results for 'all' and 'full' pores; 'full' pore is one that is not cut-off by the simulation box while 'all' pores are both 'full' pores and pores partially cut-off by the simulation box. In **Figure 4** we show the results for 'all' and 'full', and in **ESI Figure S6**, we provide the results for 'partial' pores. Because the simulation box is cubic and symmetrically centered, all 'partial' tetrahedral or octahedral pores are the same size (a small fraction of the 'full' pore). Overall, the 'full' pores contain significantly more polymer than the 'partial' pores, and the 'partial' pore trends are not drastically different from the respective 'full' pore trends. We note that the average and error are calculated by taking the average and standard deviation from 'all', just 'full', and just 'partial' tetrahedral and octahedral pores, respectively. The 'partial' pores values are much lower than the 'full' pore values, so the 'all' pore error bars are substantially larger than the error bars for just the 'full' and 'partial' pore because the 'all' pore error bars show a large deviation between the 'full' pore and 'partial' pore values.

The 'all' pore and 'full' pore data for 'Fraction of polymer beads in a pore' in **Figure 4a** and **Figure 4b**, respectively, show that the $N = 114$ polymer at both concentrations is more likely to be found near an octahedral pore rather than a tetrahedral pore. In the 'full' pore, the fraction of polymer beads in an octahedral pore is roughly thrice that in a tetrahedral pore; the 3:1 ratio of fraction of polymer beads in the pores is smaller than the ~6:1 ratio of volume of octahedral pore to tetrahedral pore. It is likely that some polymers concentrate in the smaller tetrahedral pores to enable other polymers in the octahedral pore to possess higher entropy with fewer polymer chains crowding the pore than the volume ratio would suggest. We also see that the larger polymer concentration increases the polymer localization in the smaller tetrahedral pores.

We examine the relative movement of the $N = 114$ polymer beads into and out of the different pores in **Figure 4c** and **Figure 4d**. The pore type and polymer concentration both drastically affect the number of polymer beads that move in or out of a pore. The larger octahedral pore with more polymer beads, not surprisingly, has a greater number of polymer beads moving in or out over the time interval shown. Likewise, higher polymer concentration systems possess more polymer beads enabling a larger average number of polymer beads to move between pores. When we normalize the data presented in **Figure 4c** and **Figure 4d** by the polymer concentration, we find that the normalized number of polymer beads moving between pores becomes indistinguishable between the two concentrations, for both chain lengths (**ESI Figure S7**). In **Figures 4e-4h**, the results for the $N = 228$ polymer length follow the same trends seen for the $N = 114$ polymer in **Figures 4a-4d**. For a fair comparison between the two chain lengths, we normalize the number of polymer beads moving between pores by the polymer length (**ESI Figure S7**); we find that at the same concentration, the shorter polymer has significantly more movement between pores than the longer polymer. This finding is consistent with the polymer diffusivity decrease

observed with increasing the polymer length in **Figure 3**, and the result suggests that inter-pore polymer movement is less constrained for the $N = 114$ systems compared to the $N = 228$ systems. Inter-pore polymer movement contributes more significantly to the overall polymer diffusion for the $N = 114$ systems.

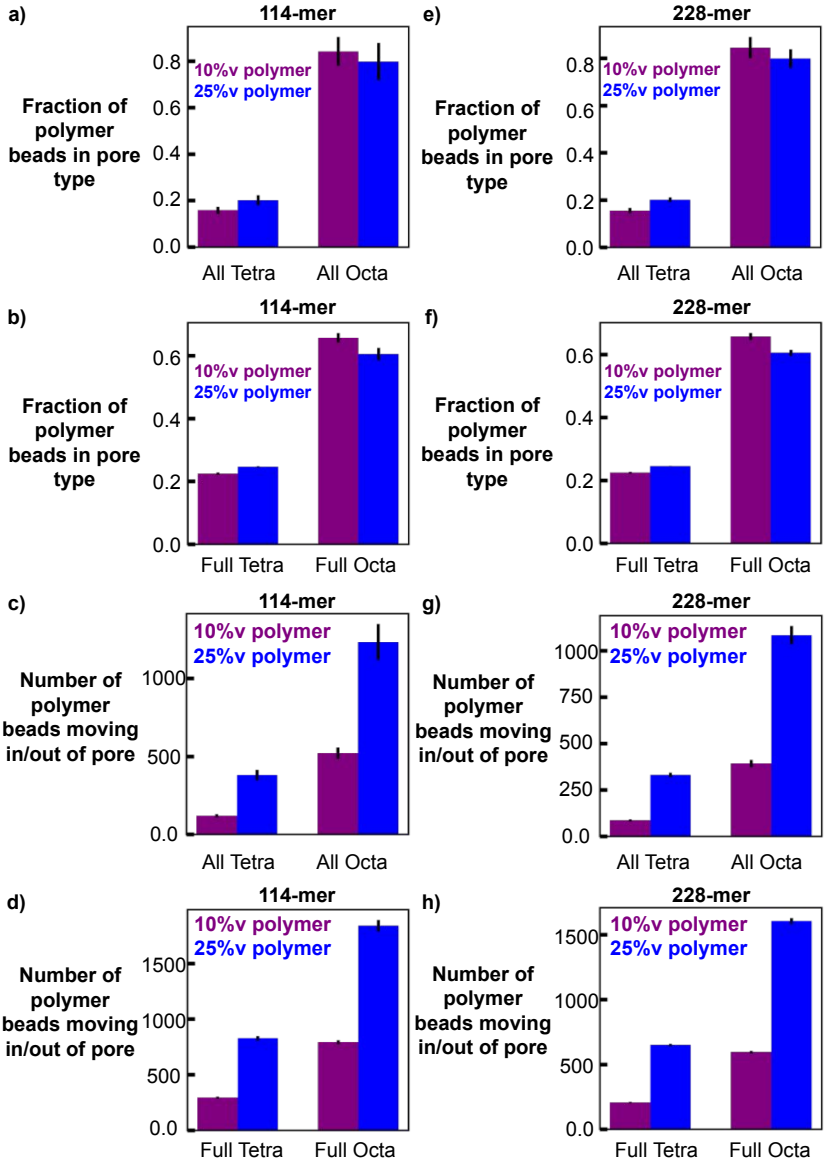

***Figure 4**: Determination of polymer localization into nearest tetrahedral or octahedral pore, and the polymer movement between pores. a), b), e), and f) describe the average fraction of all polymer beads classified as being near to a tetrahedral or octahedral pore. They provide information on*

which pores tend to have more polymer beads. Because the simulation box cuts through the HCP crystal, b) and f) elucidate the polymer localization into full pores (pore not interrupted by simulation box edge). a) and e) are then an average of both the full and partial pores. c), d, g), and h) quantify the number of all polymer beads that either enter or leave a pore over an interval of 156,250 τ. Similar to b) and f), d) and h) categorize the polymer beads movement between pores for only full pores. c) and g) are then an average of both the full and partial pores. a)-d) are for N = 114, and e)-h) are for N = 228. The error bars for all plots are the standard error of the mean of 3 independent replicates.

To understand the impact of each specific type of pore – tetrahedral and octahedral – on the polymer structure and dynamics, we perform simulations of a single tetrahedral and a single octahedral pore to compare the results from the single pore simulations to the entire HCP simulation results described so far. We focus the following section on the N = 114 and N = 228 polymer lengths because these systems have the largest CR (**Table 1**) and the 10%v and 25%v polymer concentration systems because the 1%v concentration is too low to simulate for the individual tetrahedral or octahedral pores.

B. Elucidating polymer structure and dynamics in individual tetrahedral and octahedral pores:

We quantify the polymer structure using the polymer radius of gyration in the individual tetrahedral pore and octahedral pore in **Figure 5**. **Figure 5a** and **Figure 5b** show that the N = 114 polymer at 10%v and 25%v possesses a similar P(R_g^2) profile in the octahedral pore as that in the entire HCP crystal previously shown in **Figure 2**. The P(R_g^2) profile in the tetrahedral pore exhibits one peak at smaller R_g^2 and a secondary shoulder at larger R_g^2. This profile shape results in the $\langle R_g^2 \rangle$ for the tetrahedral pore being greater than the $\langle R_g^2 \rangle$ for the octahedral pore and the entire HCP crystal in **Figure 5c**. The CR for this polymer length is below one (indicating the polymer size is smaller than the pore size) for the octahedral pore and above one for the tetrahedral pore.

Thus, we would expect the polymer in the tetrahedral pore to further collapse as indicated by the peak at lower R_g^2 or extend as it moves in or out from the tetrahedral pore, as indicated by the secondary peak at higher R_g^2.

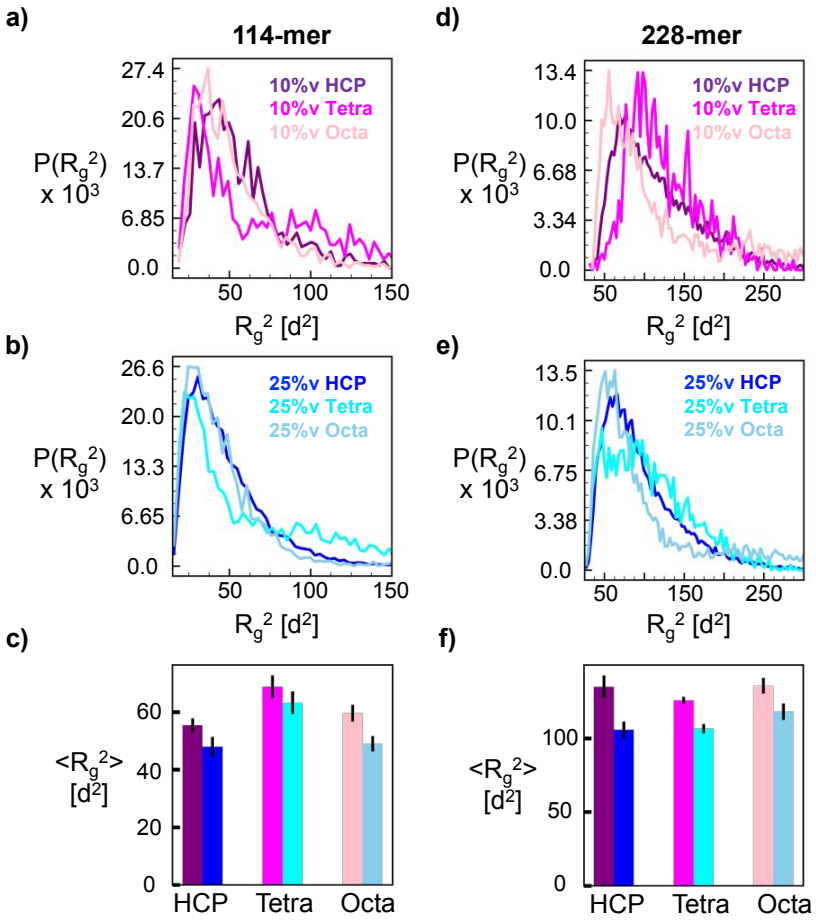

Figure 5*: Polymer radius of gyration for HCP confined, individual tetrahedral pore confined, and individual octahedral pore confined polymer solutions. a), b), d), and e) provide the squared polymer radius of gyration probability distribution as a function of the squared radius of gyration. c), and f) depict the ensemble averaged radius of gyration squared. a), b), and c) are for N = 114 polymer solutions; d), e), and f) are for N = 228 polymer solutions. The dark purple, magenta, and light pink colors are the 10%v polymer solution in the full HCP confinement, in the individual tetrahedral pore and in the individual octahedral pore respectively. The dark blue, cyan, and light blue colors are for the 25%v polymer solution in the full HCP confinement, in the individual tetrahedral pore and in the individual octahedral pore respectively. The error bars for all plots are the standard error of the mean of 3 independent replicates.*

Figure 5d, **Figure 5e**, and **Figure 5f** illustrate the polymer R_g^2 for the longest polymer considered of $N = 228$ with a greater CR than the $N = 114$ solutions; 228-mer has a CR above one for both the tetrahedral and octahedral pores with the CR being larger for the smaller tetrahedral pore (**Table 1**). Under this stronger confinement, the P(R_g^2) profile at larger R_g^2 values for the tetrahedral pore more closely matches the P(R_g^2) profile at larger R_g^2 values from the entire HCP for both the 10%v and 25%v polymer concentrations. At smaller R_g^2 values, the P(R_g^2) profile from the octahedral pore more closely matches the entire HCP confined. For both $N = 114$ and $N = 228$ polymer chains, the overall polymer structure most closely resembles the polymer structure in an octahedral pore. For the $N = 114$ polymer that has a CR below one for the octahedral pore and above unity for the tetrahedral pore, the polymer is more extended in the tetrahedral pore than it is in the overall HCP system.

Next, we study the polymer diffusion in the entire HCP crystal compared to the individual tetrahedral and octahedral pores in **Figure 6**. The $N = 114$ polymer exhibits significantly slower diffusion in the individual tetrahedral and octahedral pores compared to the entire HCP crystal (**Figure 6a** and **Figure 6b**). Not surprisingly, the polymer achieves a higher diffusion rate in the larger octahedral pore compared to the smaller tetrahedral pore due to the difference in the pore sizes. Even though the 10%v and 25%v polymer concentration systems have numerically similar diffusion rates in entire HCP, the 25%v system diffuses slightly faster than the 10%v in both the tetrahedral and octahedral pores. The minor effect of concentration on diffusivity is similar to that seen in the diffusivity results from the entire HCP system as the degree of confinement plays a more impactful role on polymer diffusion than the concentration does. The $N = 228$ polymer with higher CR exhibits similar diffusion in the entire HCP as it does in the individual pore simulations (**Figure 6c** and **Figure 6d**). Both polymer lengths in the tetrahedral pore achieve similar diffusion

rates while the longer $N = 228$ polymer in the octahedral pore diffuses slower than the shorter $N = 114$ polymer. The difference in polymer length dependence of diffusion in the different pores is caused by the polymer CR where the polymer CR in the tetrahedral pore is greater than one for both polymer lengths (~1.5 for $N = 114$; ~2.1 for $N = 228$) while the polymer CR in the octahedral pore increases from below one (~0.8) for $N = 114$ to above one (~1.2) for $N = 228$.

These findings suggest that for the $N = 114$ polymer, diffusion between pores (i.e., inter-pore diffusion) accelerates the overall diffusion rate for the confined HCP system while for the $N = 228$ polymer, the polymer diffusion in the entire HCP is dominated by the diffusion within the tetrahedral or octahedral pores with minor inter-pore diffusion. This observation follows the results from **Figure 4** and **ESI Figure S7** where a larger fraction of the polymer chain enters or leaves a pore for the $N = 114$ systems compared to the $N = 228$ systems.

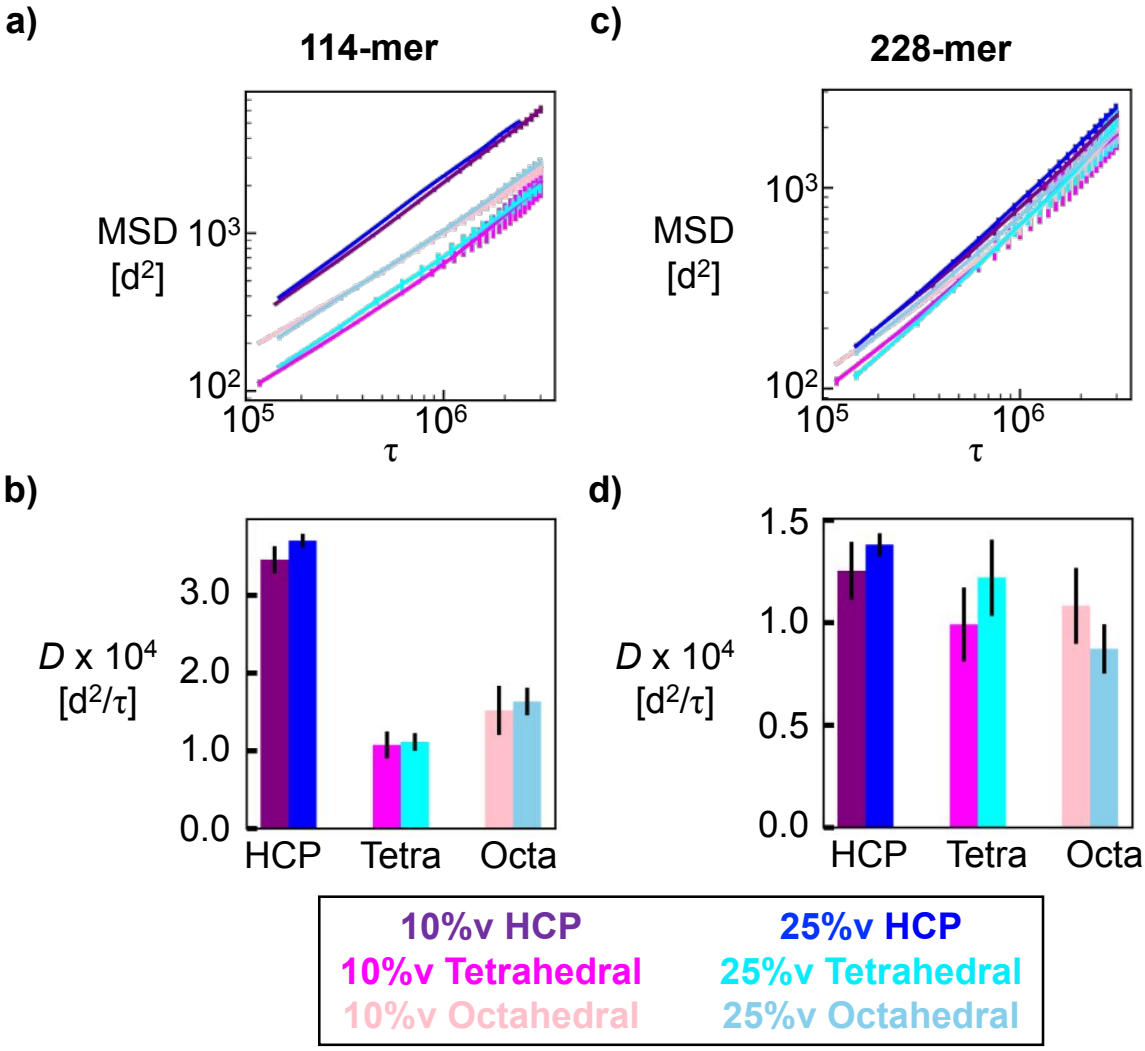

***Figure 6**: Polymer mean squared displacement (MSD) and diffusion coefficient (D) for HCP confined, individual tetrahedral pore confined, and individual octahedral pore confined polymer solutions. a) and c) provide the mean squared displacement (MSD) of the polymer COM over the simulation time τ. b), and d) depict the diffusion coefficient for each system extracted from the MSD plot. a) and b) are for N = 114 polymer solutions; c) and d) are for N = 228 polymer solutions. The dark purple, magenta, and light pink colors are the 10%v polymer solution in the full HCP confinement, in the individual tetrahedral pore and in the individual octahedral pore respectively. The dark blue, cyan, and light blue colors are for the 25%v polymer solution in the full HCP confinement, in the individual tetrahedral pore and in the individual octahedral pore respectively. The error bars for all plots are the standard error of the mean of 3 independent replicates.*

IV. Conclusion

In this work, we explore the effect of strong confinement on polymer solutions to understand how the polymer structure and dynamics change compared to bulk polymer solutions as the polymer length and concentration are varied. We focus on the good solvent regime in a hexagonally close packed (HCP) nanoparticle-based confinement with the nanoparticle sizes significantly larger than the polymer Kuhn segment sizes and with the polymer chain sizes on the order of the crystalline pore size. We show how polymer dynamics under strong HCP confinement result in trends with changing polymer concentration and lengths differing from those in the bulk. We find that in HCP confinement, polymer chains in dilute polymer concentrations exhibit significantly slowed dynamics while the polymer chains in semi-dilute polymer concentrations obtain similar polymer diffusion rates. For longer chain lengths, the overall polymer diffusion is dominated by intra-pore diffusion instead of the inter-pore diffusion that dominates at shorter chain lengths. We present a detailed view on how the structure and dynamics of polymer solution in HCP confinement is the result of an intricate interplay of individual tetrahedral and octahedral pores and the degree of confinement felt by the polymer in these pores. These results improve the understanding of polymer solution structure and diffusion through large and densely packed nanoparticle assemblies.

Author Contributions:

CRediT: **Christian M. Heil** conceptualization, investigation, data curation, formal analysis, methodology, writing-original draft; **Arthi Jayaraman** conceptualization, funding acquisition, supervision, writing-review & editing draft.

Acknowledgements:

C.M.H. and A.J. acknowledge financial support from the Air Force Office of Scientific Research (MURI-FA 9550-18-1-0142). This work was supported with computational resources from the University of Delaware (Caviness and DARWIN clusters) and the Extreme Science and Engineering Discovery Environment (XSEDE) (NSF grant ACI-1548562) Bridges-2 cluster (allocation MCB100140), which is supported by NSF award ACI-1928147. C.M.H and A.J also acknowledge J. Gilchrist (Lehigh University), R. Krishnamoorti (University of Houston), and R. Riggleman (University of Pennsylvania) for their valuable technical input on this work.

Conflicts of Interest:

The authors declare no conflicts of interest.

References:

1. L. D'Alba and M. D. Shawkey, *Physiological reviews*, 2019, **99**, 1-19.
2. F. Hussain, M. Hojjati, M. Okamoto and R. E. Gorga, *Journal of composite materials*, 2006, **40**, 1511-1575.
3. S. K. Kumar and R. Krishnamoorti, *Annual Review of Chemical and Biomolecular Engineering*, 2010, **1**, 37-58.
4. Y. Jiang, J. L. Hor, D. Lee and K. T. Turner, *ACS applied materials & interfaces*, 2018, **10**, 44011-44017.
5. Y. Qiang, S. S. Pande, D. Lee and K. T. Turner, *ACS nano*, 2022.
6. N. Jouault, D. Zhao and S. K. Kumar, *Macromolecules*, 2014, **47**, 5246-5255.
7. B. K. Kuila and A. K. Nandi, *Macromolecules*, 2004, **37**, 8577-8584.
8. S. M. Oh, M. Abbasi, T. J. Shin, K. Saalwächter and S. Y. Kim, *Physical review letters*, 2019, **123**, 167801.
9. J. R. Prakash, *Current opinion in colloid & interface science*, 2019, **43**, 63-79.
10. M. Rubinstein and R. H. Colby, *Polymer physics*, Oxford university press New York, 2003.
11. R. H. Colby, *Rheologica acta*, 2010, **49**, 425-442.
12. D. Richter and M. Kruteva, *Soft Matter*, 2019, **15**, 7316-7349.
13. E. J. Bailey and K. I. Winey, *Progress in Polymer Science*, 2020, **105**, 101242.
14. R. Chen, R. Poling-Skutvik, A. Nikoubashman, M. P. Howard, J. C. Conrad and J. C. Palmer, *Macromolecules*, 2018, **51**, 1865-1872.
15. A. Kutvonen, G. Rossi and T. Ala-Nissila, *Physical Review E*, 2012, **85**, 041803.

16. J. T. Kalathi, S. K. Kumar, M. Rubinstein and G. S. Grest, *Soft matter*, 2015, **11**, 4123-4132.
17. I. Volgin, S. Larin, A. Lyulin and S. Lyulin, *Polymer*, 2018, **145**, 80-87.
18. F. W. Starr, T. B. Schrøder and S. C. Glotzer, *Macromolecules*, 2002, **35**, 4481-4492.
19. N. Jouault, F. Dalmas, S. r. Said, E. Di Cola, R. Schweins, J. Jestin and F. o. Boué, *Macromolecules*, 2010, **43**, 9881-9891.
20. M. Crawford, R. Smalley, G. Cohen, B. Hogan, B. Wood, S. Kumar, Y. B. Melnichenko, L. He, W. Guise and B. Hammouda, *Physical review letters*, 2013, **110**, 196001.
21. A. L. Frischknecht, E. S. McGarrity and M. E. Mackay, *The Journal of chemical physics*, 2010, **132**, 204901.
22. M. E. Mackay, A. Tuteja, P. M. Duxbury, C. J. Hawker, B. Van Horn, Z. Guan, G. Chen and R. Krishnan, *Science*, 2006, **311**, 1740-1743.
23. A. Tuteja, P. M. Duxbury and M. E. Mackay, *Physical review letters*, 2008, **100**, 077801.
24. M. Vacatello, *Macromolecules*, 2001, **34**, 1946-1952.
25. N. Jouault, M. K. Crawford, C. Chi, R. J. Smalley, B. Wood, J. Jestin, Y. B. Melnichenko, L. He, W. E. Guise and S. K. Kumar, *ACS Macro Letters*, 2016, **5**, 523-527.
26. A. Winkler, D. Wilms, P. Virnau and K. Binder, *The Journal of chemical physics*, 2010, **133**, 164702.
27. A. Winkler, A. Statt, P. Virnau and K. Binder, *Physical Review E*, 2013, **87**, 032307.
28. D. Wilms, A. Winkler, P. Virnau and K. Binder, *Physical review letters*, 2010, **105**, 045701.
29. A. Statt, A. Winkler, P. Virnau and K. Binder, *Journal of Physics: Condensed Matter*, 2012, **24**, 464122.
30. S. A. Egorov, *The Journal of Chemical Physics*, 2021, **154**, 184902.
31. S. Asakura and F. Oosawa, *The Journal of chemical physics*, 1954, **22**, 1255-1256.
32. M. Muthukumar and A. Baumgärtner, *Macromolecules*, 1989, **22**, 1937-1941.
33. M. Muthukumar, *Journal of Non-Crystalline Solids*, 1991, **131-133**, 654-666.
34. J. Chuang, Y. Kantor and M. Kardar, *Physical Review E*, 2001, **65**, 011802.
35. M. Muthukumar, *The Journal of chemical physics*, 2003, **118**, 5174-5184.
36. Z. E. Dell and M. Muthukumar, *The Journal of chemical physics*, 2018, **149**, 174902.
37. S. Gam, J. S. Meth, S. G. Zane, C. Chi, B. A. Wood, M. E. Seitz, K. I. Winey, N. Clarke and R. J. Composto, *Macromolecules*, 2011, **44**, 3494-3501.
38. E. J. Bailey, R. A. Riggleman and K. I. Winey, *Macromolecules*, 2020, **53**, 8171-8180.
39. R. B. Venkatesh, T. Zhang, N. Manohar, K. J. Stebe, R. A. Riggleman and D. Lee, *Molecular Systems Design & Engineering*, 2020, **5**, 666-674.
40. R. B. Venkatesh, S. H. Han and D. Lee, *Nanoscale Horizons*, 2019, **4**, 933-939.
41. R. B. Venkatesh, N. Manohar, Y. Qiang, H. Wang, H. H. Tran, B. Q. Kim, A. Neuman, T. Ren, Z. Fakhraai and R. A. Riggleman, *Annual Review of Chemical and Biomolecular Engineering*, 2021, **12**, 411-437.
42. J. L. Hor, H. Wang, Z. Fakhraai and D. Lee, *Macromolecules*, 2018, **51**, 5069-5078.
43. J. L. Hor, H. Wang, Z. Fakhraai and D. Lee, *Soft Matter*, 2018, **14**, 2438-2446.
44. N. Manohar, K. J. Stebe and D. Lee, *Macromolecules*, 2020, **53**, 6740-6746.
45. E. Y. Lin, A. L. Frischknecht and R. A. Riggleman, *Macromolecules*, 2021.
46. H. Wang, K. L. Kearns, A. Zhang, A. Arabi Shamsabadi, Y. Jin, A. Bond, S. M. Hurney, C. Morillo and Z. Fakhraai, *Nano Letters*, 2021, **21**, 1778-1784.

47. A. Karatrantos, R. J. Composto, K. I. Winey, M. Kröger and N. Clarke, *Polymers*, 2019, **11**, 876.
48. A. Karatrantos, N. Clarke and M. Kröger, *Polymer reviews*, 2016, **56**, 385-428.
49. G. G. Vogiatzis and D. N. Theodorou, *Archives of Computational Methods in Engineering*, 2018, **25**, 591-645.
50. B. Zhang, J. Li, J. Hu and L. Liu, *Soft Matter*, 2021, **17**, 4632-4642.
51. G. S. Grest and K. Kremer, *Physical Review A*, 1986, **33**, 3628.
52. Y. Li, B. C. Abberton, M. Kröger and W. K. Liu, *Polymers*, 2013, **5**, 751-832.
53. L. V. Azaroff, *Introduction to Solids*, McGraw-Hill, 1960.
54. J. E. Jones, *Proc. R. Soc. London, Ser. A*, 1924, **106**, 463-477.
55. A. P. Thompson, H. M. Aktulga, R. Berger, D. S. Bolintineanu, W. M. Brown, P. S. Crozier, P. J. in't Veld, A. Kohlmeyer, S. G. Moore and T. D. Nguyen, *Computer Physics Communications*, 2022, **271**, 108171.
56. E. J. Maginn, R. A. Messerly, D. J. Carlson, D. R. Roe and J. R. Elliott, *Living Journal of Computational Molecular Science*, 2018, **1**, 6324.
57. W. Humphrey, A. Dalke and K. Schulten, *Journal of molecular graphics*, 1996, **14**, 33-38.
58. A. Hariharan, S. K. Kumar and T. P. Russell, *Macromolecules*, 1991, **24**, 4909-4917.